Research Article | Vol. 31, No. 22 / 23 Oct 2023 / Optics Express 36992
Optics EXPRESS

Optical adaptive power control based on atmospheric channel reciprocity for mitigating turbulence disturbances in free-space optics communication

HAIFENG YAO,[1,2,3,4,5] WEIHAO WANG,[3] CHANG ZHOU,[2] JIE CAO,[1,2] QUN HAO,[1,2,3,6] CHUNYI CHEN,[3] KEYAN DONG,[3] SHOUFENG TONG,[3] ZHI LIU,[3] XIANZHU LIU,[3] AND HUILIN JIANG[1,2,3]

[1]*Yangtze Delta Region Academy of Beijing Institute of Technology, Jiaxing 314019, China*
[2]*School of Optics and Photonics, Beijing Institute of Technology, Beijing 100081, China*
[3]*Key Laboratory of Photoelectric Measurement and Control and Optical Information Transfer Technology of Ministry of Education, Changchun University of Science and Technology, 7089 Weixing Road, Changchun 130022, China*
[4]*State Key Laboratory of Applied Optics ,Changchun Institute of Optics, Fine Mechanics and Physics, Chinese Academy of Sciences, Changchun 130033, China*
[5]*custfeng@outlook.com*
[6]*qhao@bit.edu.cn*

Abstract: A continuous time-domain adaptive power model of transmitter optical and control algorithm based on atmospheric turbulence channel reciprocity are explored for mitigating the free-space optical communication (FSOC) receiver optical intensity scintillation and bit error rate (BER) deterioration. First, a transmitter optical adaptive power control (OAPC) system architecture using four wavelength optical signals based on atmospheric turbulence channel reciprocity is proposed, and electronically variable optical attenuator (EVOA) and erbium-doped fiber amplifier (EDFA) are employed as the main OAPC units for power adaptation. Moreover, a reciprocity evaluation model for gamma-gamma (G-G) continuous-time signals is generated using the autoregressive moving average (ARMA) stochastic process, which takes into account the delay time and system noise, and a reciprocity-based OPAC algorithm is proposed. Numerical simulations were also performed to analyze the signal reciprocity characteristics under different turbulence, noise, and sampling time mismatch at both ends, as well as the scintillation index (SI) performance under OAPC system operation. Simultaneously, the time-domain signals of continuous quadrature amplitude modulation -16 (QAM-16) and QAM-32 real states are fused with the gamma-gamma (G-G) reciprocal turbulence continuous signals to analyze the probability density function (PDF) and bit error ratio (BER) performance after OAPC correction. Finally, a 64 Gpbs QAM-16 OPAC communication experiment was successfully executed based on an atmospheric turbulence simulator. It is shown that the OAPC correction is carried out using reciprocity at millisecond sampling delay, the light intensity scintillation of the communication signal can be well suppressed, the signal-to-noise ratio (SNR) is greatly improved, the suppression is more obvious under strong turbulence, the overall BER reduction is greater than 2.8 orders of magnitude with the OAPC system, and this trend becomes more pronounced as the received power increases, even reach 6 orders of magnitude in some places. This work provides real time-domain continuous signal samples for real signal generation of communication signals in real turbulence environments, adaptive coding modulation using reciprocity, channel estimation, and optical wavefront adaptive suppression, which are the basis of advanced adaptive signal processing algorithms.

#498103 https://doi.org/10.1364/OE.498103
Journal © 2023 Received 15 Jun 2023; revised 21 Sep 2023; accepted 5 Oct 2023; published 18 Oct 2023

Optics EXPRESS

1. Introduction

With the rise of intelligent online interactions, such as ChatGPT, requiring vast amounts of image, voice, and video data, optical fiber technology is now managing the majority of ground access networks and backbone networks with a total capacity of tens of Terabits per second (Tbps) [1–3]. However, the expensive hardware costs and complex geographical environments have hindered the deployment of optical fiber networks in certain rural and remote areas as well as between islands. Although mobile networks provide another reliable communication system, they are still struggling to meet the explosive growth in data demand [4,5]. In response to this issue, free-space optical communication (FSOC) technology can be utilized to bridge this gap and provide return service coverage, particularly to sparsely populated areas, through satellites and high-altitude platforms (HAP) [6,7].

However, the disturbance caused by atmospheric turbulence severely degrades the wavefront of the propagating optical beam, limiting the FSOC technology development. Therefore, new approaches are required to mitigate the bit error rate (BER) caused by turbulence perturbation. For instance, adaptive optics (AO) techniques at the receiver [8], adaptive thresholding [9,10], automatic gain control (AGC) [11], adaptive coding techniques at the transmitter [12], adaptive rate [13], adaptive power control (APC) [14,15], etc. For receiver-side adaptive processing systems, it is usually necessary to employ a large number of training sequences at the receiver end to obtain channel state information (CSI) for signal compensation processing, and these operations need to be completed within the coherence time of turbulence perturbation. However, the presence of training sequences cannot be processed in real time, resulting in high system hardware overhead and high time delay, which seriously restricts the real-time and high-speed performance of FSOC. As seen in Ref. [8], the AO system requires obtaining the detailed wavefront information of the spot at the receiver end and then feedback to adjust the deformable mirror, which is a complex control system. In Refs. [9,10], the receiver needs to be split into two optical speeds, one for channel estimation to obtain CSI and the other for adaptive thresholding. A significant amount of time is spent on processing the CSI information, which is unfavorable for fast-fading atmospheric turbulence channels. Similarly, our team has developed AGC techniques but still requires a large number of training sequences for adaptive CSI information acquisition [11].

In particular, for the transmitter adaptive techniques (see Refs. [12–15]), it is usually necessary to establish a separate radio-over-fiber (ROF) link and transmit the CSI obtained by a complex channel estimation algorithm at the Bob to Alice for adaptive control through this link. This system structure increases hardware overhead and introduces time delay, which is not conducive to high-speed communication scenarios (for the convenience of description, the two ends of FSOC are defined here as Alice and Bob). Fortunately, the researchers found that atmospheric turbulence channels are similar to radio channels (see Refs. [16,17]) in terms of reciprocity, and we can utilize this characteristic to perform channel estimation on the light waves coming from Alice to Bob, so as to obtain the CSI of the light waves propagating from Bob to Alice [18–20]. Based on this idea, Hong et al. investigated transmitter-side power adaptive techniques using APC - erbium-doped fiber amplifier (EDFA) for turbulence-tolerant FSOCs [21,22]. However, they are assuming the existence of reciprocity of the entire FSOC channel, without theoretical analysis of the reciprocity performance of the system. They only simply constructed an FSOC experiment employing on-off keying (OOK) modulation and effectively suppressed light intensity scintillation with the APC-EDFA. It is undeniable that this technology is a significant improvement. However, it has been shown that FSOC atmospheric turbulence channel is not absolutely reciprocal, and the conditions for maintaining reciprocity are strict [23–25]. For example, R. R. Parenti et. al. measured that the reciprocity of the aircraft-land slant path was maintained above 0.95 using single-mode fiber (SFM) [23]. J. Minet et. al. constructed an SMF measurement system to find reciprocity under medium-to-strong turbulence. He also obtained

Optics EXPRESS

reciprocity of γ_{12}=1 under absolute symmetry and alignment at the transmitter and receiver by phase-screen stepwise propagation simulation, but the reciprocity diminished as the two sides were not parameter mismatched [24]. D. Giggenbach et. al. experimentally observed that the reciprocity is limited by the Fresnel size $\sqrt{\lambda \cdot L}$ (λ and L denote the wavelength and propagation distance, respectively) and the reciprocity is less than 1 in the absence of an SMF receiver system [25]. In our previous work, we have theoretically and numerically simulated the existence of reciprocity in the atmospheric channel of FSOC using the SMF receiver system and measured the reciprocity to be above 0.85 in the field experiments [26–29]. The above analysis shows that in the actual experimental operation, we cannot perfectly keep the system reciprocity of FSOC at 1. Most of the similar radio channels are in the reciprocity mismatch state, which makes us unable to achieve the optimum performance of transmitter OAPC using reciprocity. Therefore, the reciprocity of atmospheric turbulence channel with FSOC transmitter OAPC system working principle and performance needs to be further studied and analyzed.

In this paper, we propose a model for FSOC transmitter OAPC systems based on the reciprocity of atmospheric turbulence channels. We also present a simulation method for spatiotemporal domain continuous communication signal generation, which can be used to analyze the performance of the OAPC system, including BER and the correction effect of optical intensity scintillation. In Section 2, the model for FSOC transmitter OAPC systems based on the reciprocity of atmospheric turbulence channels is deduced. In Section 3, the performance of the transmitter OAPC model is demonstrated and discussed. Additionally, the numerical simulation of the time-domain signal generation for FSOC's APC BER and scintillation suppression performances are also implemented and verified. In Section 4, the conclusion is elaborated.

2. FSOC transmitter OAPC model based on reciprocity

In our previous works [26–29], we constructed a reciprocity measurement system and measured that the reciprocity of a 1 km atmospheric channel could keep above 0.85. Based on the reciprocity principle, a system model is proposed for transmitter OAPC, as shown in Fig. 1. Figures 1(a) and 1(c) have the same structure, denoted as Alice and Bob, respectively. At Alice, the optical wave transmitted by LD_1 is λ_1. Digital signal $\{s_{A-M}(t)\}$ undergoes a raised-cosine filter in the arbitrary waveform generator (AWG) to generate a continuous baseband signal $s_{A-M}(t)$, which is then fed into the microwave power amplifier (MPA). By employing the lithium niobate ($LiNbO_3$) electro-optic phase modulator, the modulation signal $s_{A-M}(t)$ is loaded onto the optical wave λ_1 to generate a continuous optical baseband signal $s_{A-M\lambda_1}(t)$. After passing through the EDFA, the signal $s_{A-M\lambda_1}(t)$ is injected into the electrically variable optical attenuator (EVOA) to generate the transmitted optical signal.

It is worth noting that the EVOA can be precisely controlled by the FPGA in terms of attenuation magnitude, where the control feedback signal is obtained by the low-speed detector (low-speed PD) detecting the jittered light wave signal $\psi_{BA-\lambda_4}(t)$ coming to pass through the turbulence channel as shown in Fig. 1(b). Where, "BA" represents the transmission of the optical wave from Alice to Bob, and can also be denoted as "Bob → Alice". It can be known that the $\psi_{BA-\lambda_4}(t)$ contains the continuous time-domain fading information of the turbulent channel. $r_{BA-\lambda_2}(t)$ denotes the high-speed modulated signal for communication optical from Bob to Alice. $b_{A-\lambda_3}(t)$ denotes Alice's beacon light to indicate reciprocity calibration, acquisition, pointing, and tracking (APT).

At the transmitting antenna of the Alice, a dense wavelength division multiplexing (DWDM) is connected mainly to distinguish the received optical signal $r_{BA-\lambda_2}(t)$, transmitted optical signal $t_{AB-\lambda_1}(t)$, beacon light signal $b_{A-\lambda_3}(t)$, and the turbulence reciprocity information signal

Optics EXPRESS

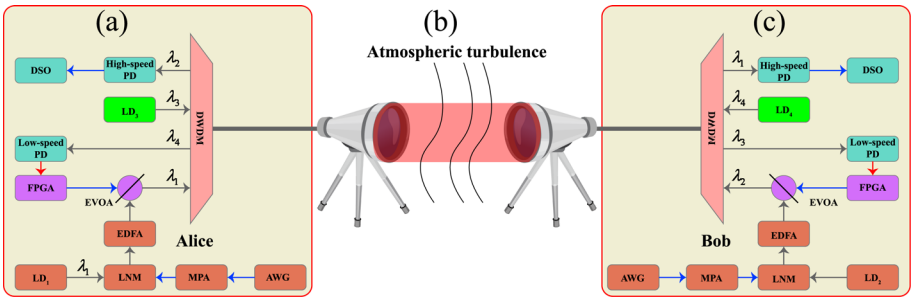

Fig. 1. OAPC system diagram for FSOC based on atmospheric turbulence channel reciprocity. (a) Optical terminal, denoted as "Alice", consists of an optical antenna, a dense wavelength division multiplexing (DWDM) system, a transmission unit, an automatic gain feedback control unit, and a detection unit. Where the sending and receiving light waves are $t_{A-\lambda_1}(t)$ and $r_{BA-\lambda_2}(t)$, respectively. The beacon light is denoted as $b_{A-\lambda_3}(t)$. $\psi_{BA-\lambda_4}(t)$ indicates the reciprocity characteristic information of the optical signal at Alice. λ_1 - λ_4 are four adjacent wavelengths in the C band. Transmission unit: laser diode (LD_1), arbitrary waveform generator (AWG), microwave power amplifier (MPA), lithium niobate modulator ($LiNbO_3$), and erbium-doped fiber amplifier (EDFA). Automatic gain feedback control unit: electrically variable optical attenuator (EVOA), field-programmable gate array (FPGA). Detection unit: fiber optic splitter (FOS), high-speed detector, digital storage oscilloscope (DSO), and low-speed detector. (b) Atmospheric turbulence channel. (c) Optical terminal, denoted as "Bob," has the same components and structure as Alice, where the sending and receiving light waves are $t_{B-\lambda_2}(t)$ and $r_{AB-\lambda_1}(t)$, respectively, the beacon light is denoted as $b_{B-\lambda_4}(t)$, $\psi_{AB-\lambda_3}(t)$ indicates the reciprocity characteristic information of the optical signal at Bob.

$\psi_{BA-\lambda_4}(t)$. The whole process can be expressed by Eqs. (1)–(2)

$$t_{A-\lambda_1}(t) = \rho_A \mu_{A-\lambda_4}(t)\, s_{A-M\lambda_1}(t) + n_A(t), \tag{1}$$

$$\mu_{A-\lambda_4}(t) \cdot \psi_{BA-\lambda_4}(t) = 1, \tag{2}$$

$$n_{\mathrm{A}} = \sigma^2_{\text{A-shot}} + \sigma^2_{\text{A-elec}} + \sigma^2_{\text{A-dark}} + \sigma^2_{\text{A-signal ,}ASE} + \sigma^2_{\text{A-ASE, ASE}}. \tag{3}$$

where $s_{A-M\lambda_1}(t) = \{s_{A-M}(t)\} \otimes g_A(t)$. $\otimes$ represents the convolution process. $g_A(t)$ denotes the matched filter, which is typically comprised of up-sampling and down-sampling raised cosine filters. ρ_A is the index of EDFA amplification at the Alice. $n_A(t)$ represents signal noise, which include the shot noise ($\sigma^2_{\text{A-shot}}$), the electronic noise ($\sigma^2_{\text{A-elec}}$), and the dark current noise ($\sigma^2_{\text{A-dark}}$) for the detector, the interactions between signals and amplified spontaneous emission (ASE) noise ($\sigma^2_{\text{A-signal, ASE}}$) for the EDFA as well as between ASE and ASE noise itself ($\sigma^2_{\text{A-ASE, ASE}}$). They can be equivalent to the additive white noise (AWGN) in the linear operating region where the Alice electronics are located as described in Fig. 1 (see, [30], Chaps. 7-12). $\mu_{A-\lambda_4}(t)$ denotes the gain-adjustable signal generated by the field-programmable gate array (FPGA), which primarily utilizes the EVOA to generate an automatically adjusted optical signal $t_{A-\lambda_1}(t)$ that suppresses the received optical power jitter. It is worth noting that $\mu_{A-\lambda_4}(t)$ is a time-varying continuous feedback signal with low time delay in practical engineering, and its accurate generation is especially important in this model, which can be obtained by detecting the fading characteristics of turbulence signal $\psi_{BA-\lambda_4}(t)$ by low-speed photodetector and processing in FPGA.

It is known from our previous work that $\psi_{BA-\lambda_4}(t)$ and $\psi_{AB-\lambda_3}(t)$ are a pair of reciprocal optical signals with continuous time-varying spatial and temporal domains after propagating turbulence channel. Therefore, it is necessary to analyze the reciprocity between them. In order to keep the fading characteristics of light waves consistent, four wavelengths of adjacent wavelengths in

Optics EXPRESS

the C-band can be used as communication light and beacon light in practical engineering [26]. Here the $\psi_{BA-\lambda_4}(t)$ signal is received by the detector and is sampled as a collection of digital sequences of the form $\left\{\Psi_{BA-\lambda_4-1}, \Psi_{BA-\lambda_4-2}, \ldots, \Psi_{BA-\lambda_4-n}\right\} = \mathbf{\Psi}_{BA-\lambda_4}$, whose power spectral density (PSD) function $S_{\psi_{BA-\lambda_4}}(\omega)$ can be regarded as a process that describes white noise of power σ_n^2 through a transfer function $H_{\psi_{BA-\lambda_4}}(\omega)$ rational filter, as show in Eq. (4)

$$\begin{aligned} S_{\psi_{BA-\lambda_4}}(\omega) &= \sum_{n=1}^{\infty} R_{\psi_{BA-\lambda_4}}(n) e^{-j\omega n} \\ &= \left|\frac{B_{\psi_{BA-\lambda_4}}(\omega)}{A_{\psi_{BA-\lambda_4}}(\omega)}\right| \sigma_n^2 = H_{\psi_{BA-\lambda_4}}(\omega)\, \sigma_n^2 \end{aligned}. \tag{4}$$

where $R_{\psi_{BA-\lambda_4}}(n)$ represents the digital signal form of the auto covariance function (ACF) of the signal. $A_{\psi_{BA-\lambda_4}}(\omega) = 1 + a_1 e^{-j\omega} + \cdots a_n e^{-jn\omega}$, $B_{\psi_{BA-\lambda_4}}(\omega) = 1 + b_1 e^{-j\omega} + \cdots b_m e^{-jm\omega}$, where a_i is the filter coefficient of the transfer function for the atmospheric turbulence channel.

According to our previous work [31], Eq. (4) could be solved by utilizing the autoregressive moving average (ARMA) process. Therefore, we have:

$$\begin{cases} R_{\psi_{BA-\lambda_4}}(0) + \sum\limits_{n=1}^{N} a_i R_{\psi_{BA-\lambda_4}}(-n) = \sigma^2 \\ R_{\psi_{BA-\lambda_4}}(m) + \sum\limits_{n=1}^{N} a_n R_{\psi_{BA-\lambda_4}}(m-n) = 0 \end{cases}, \tag{5}$$

$$\begin{aligned} \mathbf{R}_{\psi_{BA-\lambda_4},n+1} \begin{bmatrix} 1 \\ \theta_n \end{bmatrix} &= \begin{bmatrix} \sigma_n^2 \\ 0 \end{bmatrix} \\ &= \begin{bmatrix} R_{\psi_{BA-\lambda_4}}(0) & R_{\psi_{BA-\lambda_4}}(-1) & \cdots & R_{\psi_{BA-\lambda_4}}(-n) \\ R_{\psi_{BA-\lambda_4}}(1) & R_{\psi_{BA-\lambda_4}}(0) & & \vdots \\ \vdots & & \ddots & R_{\psi_{BA-\lambda_4}}(-1) \\ R_{\psi_{BA-\lambda_4}}(n) & \cdots & & R_{\psi_{BA-\lambda_4}}(0) \end{bmatrix} \begin{bmatrix} 1 \\ a_1 \\ \vdots \\ a_n \end{bmatrix} \end{aligned}. \tag{6}$$

By employing the order recursive solution of the Yule-Walker function, the time-dependent series $\{I_1, I_2, \ldots I_n\} = \mathbf{I}$ can be obtained by solving Eqs. (5) and (6), as shown in Eqs. (7)–(9). Note that the $\mathbf{I}$ at this point does not have fusion probability density function (PDF) characteristics.

$$\theta_{n+1} = \begin{bmatrix} \theta_n \\ 0 \end{bmatrix} + \xi_{n+1} \begin{bmatrix} \theta_n \\ 1 \end{bmatrix}, \quad {\sigma^2}_n \theta_n = I_n, \tag{7}$$

$$\sigma_{n+1}^2 = \sigma_n^2 \left(1 - |\xi_{n+1}|^2\right), \tag{8}$$

$${\sigma^2}_n H(\omega) = I_n. \tag{9}$$

where $\xi_{n+1} = -\alpha_n / \sigma_n^2$. The gamma-gamma (G-G) function as the PDF for turbulence channels. The parameters α and β of this function can be associated with the turbulence intrinsic parameter

Optics EXPRESS

C_n^2, as shown in Eqs. (10)–(12) [31,32],

$$p_I\left(\psi_{BA-\lambda_4}\right) = \frac{2(\alpha\beta)^{(\alpha+\beta)/2}}{\Gamma(\alpha)\Gamma(\beta)\psi_{BA-\lambda_4}}\left(\frac{\psi_{BA-\lambda_4}}{\left\langle\psi_{BA-\lambda_4}\right\rangle}\right)^{(\alpha+\beta)/2} \times K_{\alpha-\beta}\left(2\sqrt{\frac{\alpha\beta\psi_{BA-\lambda_4}}{\left\langle\psi_{BA-\lambda_4}\right\rangle}}\right), \psi_{BA-\lambda_4}>0 \quad , \tag{10}$$

$$\alpha = \frac{1}{\sigma_X^2} = \frac{1}{\exp(\sigma_{\ln X}^2)-1} \quad \beta = \frac{1}{\sigma_Y^2} = \frac{1}{\exp(\sigma_{\ln Y}^2)-1} \quad , \tag{11}$$

$$\sigma_{\ln X}^2 = \frac{0.49\sigma_R^2}{\left(1+1.11\sigma_R^{12/5}\right)^{7/6}}, \quad \sigma_{\ln Y}^2 = \frac{0.51\sigma_R^2}{\left(1+0.69\sigma_R^{12/5}\right)^{5/6}} \quad . \tag{12}$$

where $\left\langle{\psi_{BA-\lambda_4}}^n\right\rangle = \int_{-\infty}^{+\infty} p_I\left(\psi_{BA-\lambda_4}\right)\left(\psi_{BA-\lambda_4}\right)^n d\psi_{BA-\lambda_4}$ represents the n^{th} moment of signal $\psi_{BA-\lambda_4}(t)$, and $\Gamma(\cdot)$ is the gamma function. We assume that the normalized random optical power signal sequences $\left\{\widehat{\Psi}_{BA-\lambda_4-n}/\left\langle\widehat{\boldsymbol{\Psi}}_{BA-\lambda_4}\right\rangle\right\}_{1\times N}$ obey the gamma-gamma PDF. $\widehat{\boldsymbol{\Psi}}_{BA-\lambda_4}$ is rearranged in the order of $\mathbf{I}$ to obtain $\overrightarrow{\boldsymbol{\Psi}}_{BA-\lambda_4}$, so that we have mapped the time-dependent information of $\mathbf{I}$ perfectly to $\overrightarrow{\boldsymbol{\Psi}}_{BA-\lambda_4}$, and satisfy

$$\begin{cases} \overrightarrow{\boldsymbol{\Psi}}_{BA-\lambda_4} \in PDF_{Gamma-Gamma} \\ \underbrace{\left\langle\left(\overrightarrow{\Psi}_{BA-\lambda_4-i} - \left\langle\overrightarrow{\boldsymbol{\Psi}}_{BA-\lambda_4}\right\rangle\right)\left(\overrightarrow{\Psi}_{BA-\lambda_4-(i-m)} - \left\langle\overrightarrow{\boldsymbol{\Psi}}_{BA-\lambda_4}\right\rangle\right)\right\rangle}_{R_{\overrightarrow{\boldsymbol{\Psi}}_{BA-\lambda_4}}(m)} = R_{\psi_{BA-\lambda_4}}(m) \end{cases} \quad . \tag{13}$$

Equation (13) also means that the ACF $R_{\overrightarrow{\boldsymbol{\Psi}}}(m)$ of the generated $\overrightarrow{\boldsymbol{\Psi}}_{BA-\lambda_4}$ is equal to the numerical solution $R_{\psi_{BA-\lambda_4}}(m)$ of the theoretical solution equation, and no PDF information is lost. Similarly, the digital sequence signal $\overrightarrow{\boldsymbol{\Psi}}_{AB-\lambda_3}$ of the $\psi_{AB-\lambda_3}(t)$ signal can be found according to Eqs. (4)–(13).

To evaluate their relationship better, the correlation coefficient (CC) is used to measure the degree of reciprocity, as shown in Eq. (14):

$$\eta_{AB} = \eta_{BA} = \mathrm{CC}\left(\psi_{BA-\lambda_4}(t), \psi_{AB-\lambda_3}(t)\right) = \frac{\left\langle\left(\psi_{BA-\lambda_4}(t)-\left\langle\psi_{BA-\lambda_4}(t)\right\rangle\right)\left(\psi_{AB-\lambda_3}(t)-\left\langle\psi_{AB-\lambda_3}(t)\right\rangle\right)\right\rangle}{\sqrt{\left\langle\left(\psi_{BA-\lambda_4}(t)-\left\langle\psi_{BA-\lambda_4}(t)\right\rangle\right)^2\right\rangle\left\langle\left(\psi_{AB-\lambda_3}(t)-\left\langle\psi_{AB-\lambda_3}(t)\right\rangle\right)^2\right\rangle}}. \tag{14}$$

However, in practical scenarios, the noise of the detector and the signal acquisition time is not synchronized causing reciprocity mismatch, i.e., $\eta_{AB} \neq 1$. In order to describe the above relationship more accurately, by rewriting Eq. (14), we can obtain

$$\eta_{AB} = \mathrm{CC}\left(\psi_{BA-\lambda_4}(t+\tau_d) + n_{A-Low}(t), \psi_{AB-\lambda_3}(t) + n_{B-Low}(t)\right). \tag{15}$$

where τ_d is the relative delay time between Alice and Bob, $n_{A-Low}(t)$ and $n_{B-Low}(t)$ denote the noise of Alice's and Bob's low-speed detectors, and the noise of other electronics, respectively. Equations (14) and (15) are equivalent when the signal-to-noise ratio (SNR) of the system is optimal and the reciprocal turbulence signals are sampled synchronously. Therefore, a high SNR and synchronous sampling detection system are required in practical engineering.

By comparing Eqs. (2) and (15), it is found that the $\mu_{A-\lambda_4}(t)$ at Alice is to calibrate the jitter caused by the signal $s_{A-M\lambda_1}(t)$ at Bob passing through the atmospheric turbulence channel, and

Optics EXPRESS

the conventional practice is to obtain the CSI at Bob and then correct it. Theoretically, there exists

$$\mu_{A-\lambda_4}(t) \cdot \psi_{AB-\lambda_3}(t) = 1. \tag{16}$$

However, in practical scenarios, it is necessary to obtain many training sequences and perform CSI extraction. Since atmospheric turbulence is a continuous and fast-changing process in the spatiotemporal domain, there is a high delay in principle, the channel state cannot be accurately estimated, and the real-time processing of high-speed signals cannot be performed to reduce the BER. In this paper, based on this problem, the reciprocity can be utilized to obtain the CSI of the Alice → Bob light beam propagation process in real time. Specifically, we have

$$\eta_{AB} = 1, \tag{17}$$

$$\psi_{AB-\lambda_3}(t) = \psi_{BA-\lambda_4}(t), \tag{18}$$

$$\mu_{A-\lambda_4}(t) \cdot \psi_{BA-\lambda_4}(t) = \mu_{A-\lambda_4}(t)\,\psi_{AB-\lambda_3}(t). \tag{19}$$

Hence, the attenuation coefficient of the EVOA at Alice in Fig. 1 can be adjusted by acquiring the optical signal $\psi_{BA-\lambda_4}(t)$ from Bob → Alice. The CSI of Alice → Bob can be obtained in real-time by utilizing reciprocity, and the automatic gain factor $\mu_{A-\lambda_4}(t)$ can be calculated, that is, the automatic gain adjustment of the transmission power as in Eq. (1) is implemented, which can suppress signal scintillation caused by turbulence disturbance, and reduce the BER.

3. Theoretical model analysis for FSOC transmitter OAPC

Before analyzing the reciprocal characteristics of the turbulent signal, we plotted the 1-second-long $\psi_{BA-\lambda_4}(t)$ continuous time-domain waveform $\overrightarrow{\mathbf{\Psi}}_{BA-\lambda_4}$ according to Eqs. (4)–(13), as shown in Fig. 2. To maintain continuity, the simulation conditions were set in accordance with those in Ref. [31]. The turbulence intensities are set to $C_n^2 = 5 \times 10^{-14}$ m$^{-2/3}$, $C_n^2 = 5 \times 10^{-15}$ m$^{-2/3}$, and $C_n^2 = 5 \times 10^{-16}$ m$^{-2/3}$, corresponding to the strong Fig. 2(a), medium Fig. 2(b), and weak Fig. 2(c) turbulence scenarios, respectively. In this paper, the optical wavelengths are set to $\lambda_1 = 1550.12$ nm, $\lambda_2 = 1550.52$ nm, $\lambda_3 = 1550.92$ nm and $\lambda_4 = 1551.32$ nm, respectively. Moreover, the propagation distance, the transverse wind speed, and system noise are set to $L = 5000$ m, $v_\perp = 1$ m/s, and $n_A = n_B = 0$.

The Rytov variances of turbulence under these three conditions are 19.03, 1.903, and 0.19, respectively, corresponding to the strong, medium, and weak turbulence scenarios. We statistically analyzed the simulated data and obtained the scintillation indexes (SIs) of 1.1869, 0.9445, and 0.1845 for the three turbulent states according to Eq. (20). It can be concluded that the SI decreases and the fluctuation amplitude decreases as the degree of turbulence increases.

$$\sigma^2_{\psi_{BA-\lambda_4}} = \sigma^2_{\overrightarrow{\mathbf{\Psi}}_{BA-\lambda_4}} = \left(\left\langle \overrightarrow{\mathbf{\Psi}}^2_{BA-\lambda_4} \right\rangle - \left\langle \overrightarrow{\mathbf{\Psi}}_{BA-\lambda_4} \right\rangle^2\right) \Big/ \left\langle \overrightarrow{\mathbf{\Psi}}_{BA-\lambda_4} \right\rangle^2. \tag{20}$$

According to Eq. (15), knowing that time delay τ_d is an important factor, we analyze the three turbulent signals shown in Fig. 2 and plot the relationship between the effect of sampling time delay on reciprocity at Alice and Bob, as shown in Fig. 3. Where blue,black and red lines represent $C_n^2 = 5 \times 10^{-14}$ m$^{-2/3}$, $C_n^2 = 5 \times 10^{-15}$ m$^{-2/3}$ and $C_n^2 = 5 \times 10^{-16}$ m$^{-2/3}$, respectively.

Observing Fig. 3, we can know that as the turbulence delay time τ_d increases, the CC decreases and gradually approaches 0, indicating that the correlation between $\psi_{AB-\lambda_3}(t)$ and $\psi_{BA-\lambda_4}(t)$ optical signal sequences decreases. This also indicates that atmospheric turbulence is a random process in the spatiotemporal domain, leading to irregular random fluctuations of optical intensity

Optics EXPRESS

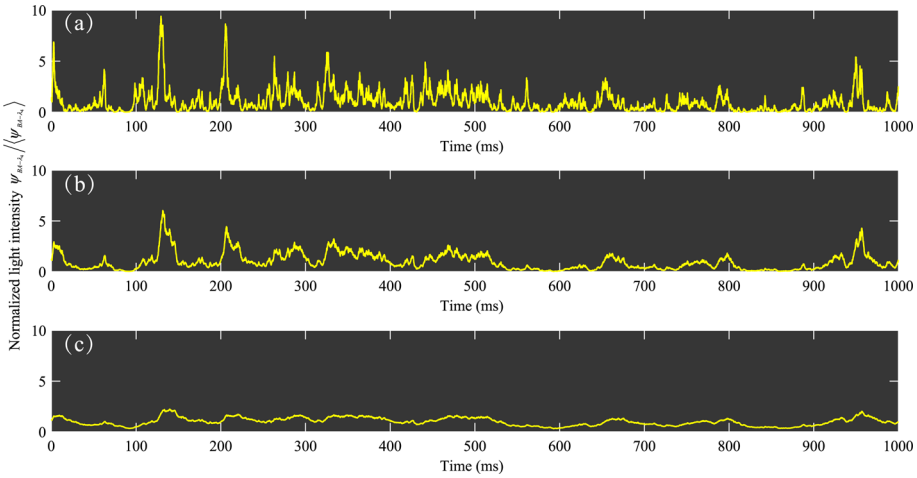

Fig. 2. Continuous time-domain optical signal waveforms for different turbulence scenarios. The turbulence intensities are set to (a) $C_n^2 = 5 \times 10^{-14}$ m$^{-2/3}$, (b) $C_n^2 = 5 \times 10^{-15}$ m$^{-2/3}$, and (c) $C_n^2 = 5 \times 10^{-16}$ m$^{-2/3}$. The four optical wavelengths are $\lambda_1 = 1550.12$ nm, $\lambda_2 = 1550.52$ nm, $\lambda_3 = 1550.92$ nm and $\lambda_4 = 1551.32$ nm, respectively. The propagation distance, the transverse wind speed, and system noise represent $L = 5000$ m, $v_\perp = 1$ m/s, and $n_A = n_{B-Low} = 0$.

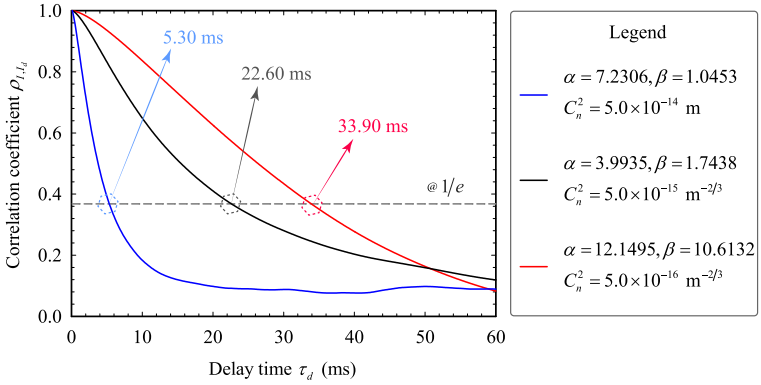

Fig. 3. Reciprocity performance of Alice and Bob optical signal sequences under different turbulences and sampling delays. Blue, black, and red lines denote $C_n^2 = 5 \times 10^{-14}$ m$^{-2/3}$, $\alpha = 7.2306$, $\beta = 1.0453$; $C_n^2 = 5 \times 10^{-15}$ m$^{-2/3}$, $\alpha = 3.9935$, $\beta = 1.7438$; and $C_n^2 = 5 \times 10^{-16}$ m$^{-2/3}$, $\alpha = 12.1495$, $\beta = 10.6132$. The four optical wavelengths are $\lambda_1 = 1555.75$ nm, $\lambda_2 = 1554.13$ nm, $\lambda_3 = 1552.52$ nm, and $\lambda_4 = 1548.51$ nm, respectively. The propagation distance, the transverse wind speed, and system noise represent $L = 5000$ m, $v_\perp = 1$ m/s, and $n_A = n_B = 0$.

as well. In practical engineering, $1/e$ is usually adopted as a maintenance condition of reciprocity, which can be expressed as [26,31]

$$\eta_{AB} \Rightarrow \begin{cases} \text{Reciprocity}, & \eta_{AB} \geq 1/e \\ \text{Non} - \text{reciprocity}, & \eta_{AB} < 1/e \end{cases}. \tag{21}$$

According to Eq. (21), when channel is strong turbulence, i.e., $C_n^2 = 5 \times 10^{-14}$ m$^{-2/3}$, the reciprocity decreases sharply as the relative sampling delay time τ_d increases at both Alice and

Optics EXPRESS

Bob and the reciprocity is mismatched after 5.30 ms, as shown by the blue line in Fig. 3. However, as the degree of turbulence decreases, the reciprocity retention time is prolonged, as depicted by the black and red lines in Fig. 3. For the medium and weak two turbulence intensities, the reciprocity retention times are 22.60 ms and 33.90 ms, respectively.

In practical communication systems, time delays are typically maintained at the millisecond level to ensure high-speed transmission of information [33]. Therefore, the time-continuous signal reciprocity evaluation model proposed in this paper can accurately characterize the relationship between reciprocity and delay time. The SNR of the detector is another major factor that affects reciprocity. The CCs between $\psi_{AB-\lambda_3}(t)$ and $\psi_{BA-\lambda_4}(t)$ optical signal sequences with different SNRs under three types of turbulence are investigated in our study to reflect their reciprocity performance, as shown in Fig. 4. For weak turbulence, the CC is enhanced from 0.575 to 0.996 when the SNR increases from 5 dB to 30 dB. Afterward, it tends to approach 1 and reaches an ideal saturation state, which means that the detector SNR needs to be kept above 30 dB if we want to obtain the perfect reciprocity between $\psi_{AB-\lambda_3}(t)$ and $\psi_{BA-\lambda_4}(t)$ signals, as shown by the red line in Fig. 4. Similarly, the similar phenomenon exists under medium and strong turbulence, as shown by the black and blue lines in Fig. 4.

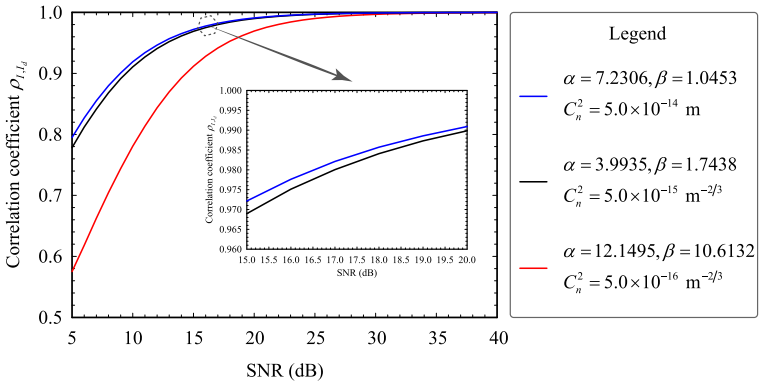

Fig. 4. Reciprocity performances of Alice and Bob optical signal sequences under different turbulences and SNRs. Blue, black, and red lines denote $C_n^2 = 5 \times 10^{-14}$ m$^{-2/3}$, $\alpha = 7.2306$, $\beta = 1.0453$; $C_n^2 = 5 \times 10^{-15}$ m$^{-2/3}$, $\alpha = 3.9935$, $\beta = 1.7438$; and $C_n^2 = 5 \times 10^{-16}$ m$^{-2/3}$, $\alpha = 12.1495$, $\beta = 10.6132$. The four optical wavelengths are $\lambda_1 = 1555.75$ nm, $\lambda_2 = 1554.13$ nm, $\lambda_3 = 1552.52$ nm, and $\lambda_4 = 1548.51$ nm, respectively. The propagation distance, the transverse wind speed, and sampling delay time represent $L = 5000$ m, $v_\perp = 1$ m/s, and $\tau_d = 0$.

This demonstrates that to obtain the same perfect reciprocity, i.e., $\eta_{AB} = 1$, for the medium-intensity turbulence in this paper, the SNR needs to be kept just at 25 dB. Due to the large degree of undulation in medium to strong turbulence, it is not sensitive to noise, as shown in Fig. 2(b) and Fig. 2(c). For weak turbulence, the degree of random jitter of the signal increases as the noise increases, leading to a decrease in reciprocity, thus the weaker the turbulence, the more sensitive it is to noise. It also shows that the reciprocity degrades as the degree of turbulence increases under the same SNR condition. In addition, the CCs of all three turbulent states in Fig. 4 are greater than $1/e$, indicating that the $\psi_{AB-\lambda_3}(t)$ and $\psi_{BA-\lambda_4}(t)$ optical signal sequences are reciprocal at SNR greater than 5 dB. At a certain degree of turbulence, the CC will be in saturation with the increase of SNR.

The purpose of this paper is to achieve OAPC at the transmitter. Therefore, according to Eqs. (1)–(15), the Monte Carlo numerical simulations are carried out to generate the spatiotemporal domain continuous signal $t_{A-\lambda_1}(t)$. It is worth noting that in practical engineering, the optical gain cannot be increased infinitely, and considering the existence of saturation of the detector, we

Optics EXPRESS

assume that the maximum detectable optical gain of the low-speed detector in Fig. 1 is 25 dB and is in the optimal operating condition. Where the photocurrent in the saturated state is 2 times that of max $\left(\psi_{BA-\lambda_4}(t)\right)$ and is in the detectable range of 25 dB, hence Eqs. (2) and (16) exist

$$\mu_{A-\lambda_4}(t)=\begin{cases}1/\psi_{BA-\lambda_4}(t), & 1/\psi_{BA-\lambda_4}(t)<25\text{dB}\\ 25\text{ dB}, & \text{Others}\end{cases}, \tag{22}$$

$$\mu_{A-\lambda_4}(t)\cdot\psi_{BA-\lambda_4}(t)=\begin{cases}Still, & \mu_{A-\lambda_4}(t)\cdot\psi_{BA-\lambda_4}(t)\le 2\cdot\max\left(\psi_{BA-\lambda_4}(t)\right)\\ 2\cdot\max\left(\psi_{BA-\lambda_4}(t)\right), & \text{Others}\end{cases}. \tag{23}$$

In addition, to better evaluate the correction depth χ_{dB} of the SI, it is defined as

$$\chi_{dB}=10\log_{10}\left(\sigma^2_{r_{AB-\lambda_1}}-\sigma^2_{r_{AB-\lambda_1-Turb}}\right)\Big/\sigma^2_{r_{AB-\lambda_1-Turb}}. \tag{24}$$

where $\sigma^2_{r_{AB-\lambda_1-Turb}}=\sigma^2_{\psi_{AB-\lambda_3}}$. The signal $s_{A-M\lambda_1}(t)$ propagated from Alice to Bob through the atmospheric turbulence channel is denoted as $r_{AB-\lambda_1-Turb}(t)$, while the signal transmitted through OAPC correction utilizing $\mu_{A-\lambda_4}(t)$ is denoted as $r_{AB-\lambda_1}(t)$, which can be written

$$r_{AB-\lambda_1-Turb}(t)=\rho_A\psi_{AB-\lambda_1}(t)\,s_{A-M\lambda_1}(t)+n_A(t), \tag{25}$$

$$\begin{aligned}r_{AB-\lambda_1}(t)&=\mu_{A-\lambda_4}(t)\left[\rho_A\psi_{AB-\lambda_1}(t)\,s_{A-M\lambda_1}(t)+n_A(t)\right]\\&=\psi_{AB-\lambda_1}(t)\,t_{A-\lambda_1}(t).\end{aligned} \tag{26}$$

Combining Eqs. (15)–(24) , the performances of the transmitter OAPC are investigated using reciprocity at different sampling time delays, as plotted in Fig. 5. For strong turbulence $C_n^2=5\times10^{-14}$ m$^{-2/3}$, it was observed that the SI sharply increases with an increase in delay time τ_d. When the delay time exceeds 5.30 ms, the SI is found to be in the saturation region, approximately 1.60, as shown by the blue line in Fig. 5. It is noteworthy that, 5.30 ms is also the maintaining condition of reciprocity for strong turbulence. This indicates that within the reciprocity time, the OAPC can effectively suppress the jitter of the detector receiving signal caused by turbulence disturbance. Furthermore, the SI $\sigma^2_{r_{AB-\lambda_1}}$ at the point where the delay time τ_d is 0. It shows that the light wave emitted from Alice propagates through the atmospheric channel to Bob and the light intensity jitter can be completely suppressed theoretically. It is also required that the system shown in Fig. 1, in practical operation, requires the sampling times at both Alice and Bob to be kept synchronized. The same properties are present when the turbulence is medium $C_n^2=5\times10^{-15}$ m$^{-2/3}$ and weak $C_n^2=5\times10^{-16}$ m$^{-2/3}$, as shown by the black and red lines in Fig. 5.

Additionally, in the portion where the reciprocity is maintained, the slopes of the blue, black, and red curves in Fig. 5 are approximately 0.307, 0.060, and 0.075, respectively. This indicates that the weaker the turbulence, the more sensitive the corrected SI is to the time delay, i.e., the relative SI suppression effect slows down as the turbulence intensity increases within the same delay time. For instance, when the delay time is $\tau_d=1$ ms and strong turbulence $C_n^2=5\times10^{-14}$ m$^{-2/3}$, there is $\sigma^2_{r_{AB-\lambda_1-Turb}}=1.1869\xrightarrow{\downarrow\chi_{dB}=-3.5\text{ dB}}\sigma^2_{r_{AB-\lambda_1}}=0.6334$; with medium turbulence $C_n^2=5\times10^{-15}$ m$^{-2/3}$, there is $\sigma^2_{r_{AB-\lambda_1-Turb}}=0.9445\xrightarrow{\downarrow\chi_{dB}=-0.18\text{ dB}}\sigma^2_{r_{AB-\lambda_1}}=0.0395$; with weak turbulence $C_n^2=5\times10^{-16}$ m$^{-2/3}$, there is $\sigma^2_{r_{AB-\lambda_1-Turb}}=0.1845\xrightarrow{\downarrow\chi_{dB}=-0.047\text{ dB}}\sigma^2_{r_{AB-\lambda_1}}=0.002$. This also exactly validates the perfect reciprocal state information extraction in Fig. 3, which requires the system Alice and Bob to have simultaneous sampling capabilities.

Optics EXPRESS

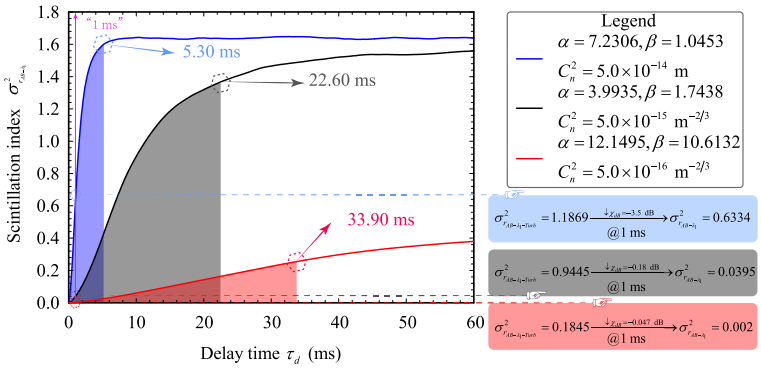

Fig. 5. SI performances of reciprocity optical signal sequences at Alice and Bob after OAPC calibration under different turbulences and sampling delays. Blue, black, and red lines denote $C_n^2 = 5\times10^{-14}$ m$^{-2/3}$, $\alpha = 7.2306$, $\beta = 1.0453$; $C_n^2 = 5\times10^{-15}$ m$^{-2/3}$, $\alpha = 3.9935$, $\beta = 1.7438$; and $C_n^2 = 5\times10^{-16}$ m$^{-2/3}$, $\alpha = 12.1495$, $\beta = 10.6132$. The four optical wavelengths are $\lambda_1 = 1555.75$ nm, $\lambda_2 = 1554.13$ nm, $\lambda_3 = 1552.52$ nm, and $\lambda_4 = 1548.51$ nm, respectively. The propagation distance, the transverse wind speed, and system noise represent $L = 5000$ m, $v_\perp = 1$ m/s, and $n_A = n_B = 0$.

Comparing with Fig. 4, the SI performances of reciprocal optical signal sequences at Alice and Bob after OAPC calibration under different SNRs are investigated, as shown in Fig. 6. Where $\tau_d = 0$ ms. The blue, black, and red dashed and solid lines represent uncalibrated and calibrated SI of optical signals propagated from Alice to Bob under strong $C_n^2 = 5\times10^{-14}$ m$^{-2/3}$, medium $C_n^2 = 5\times10^{-15}$ m$^{-2/3}$, and weak $C_n^2 = 5\times10^{-14}$ m$^{-2/3}$ turbulence conditions, respectively. It can be observed that the correction using a reciprocal signal is effective in suppressing light intensity scintillation. Under the same turbulence condition, the ability of the OAPC to suppress the optical intensity jitter first decreases and then increases with the increase of SNR. This phenomenon is plotted in Fig. 6(a). For strong turbulence conditions, there is a minimum correction ability of 4.762 dB at $SNR = 27$ dB, which can be depicted as $\sigma^2_{r_{AB-\lambda_1-Turb}} = 1.1913 \xrightarrow{\downarrow\chi_{dB}=-4.762\ \mathrm{dB}} \sigma^2_{r_{AB-\lambda_1}} = 0.7934$ @ $SNR = 27$ dB, meaning that the correction capacity at this time is weak. After the fusion of noise and optical signals, the system is in a state of entropy saturation. Consequently, when using reciprocity-based automatic gain control, the SI gradually approaches a saturation state. Under medium $C_n^2 = 5\times10^{-15}$ m$^{-2/3}$ and weak $C_n^2 = 5\times10^{-16}$ m$^{-2/3}$ turbulence conditions, there are also minimum points of scintillation correction depth χ_{dB}, which are -3.716 dB and -1.7690 dB, respectively. These phenomenons of BER comparison before and after OAPC calibration of Alice and Bob reciprocal optical signal sequences under different SNRs are depicted in Fig. 8.

The purpose of this paper is to utilize reciprocity to perform automatic gain control on the optical signal $s_{A-M\lambda_1}(t)$ at the Alice, thereby suppressing the optical intensity scintillation caused by turbulence disturbance. Considering the transmission rate, the noise equivalent power (NEP) of the detector, and the SNR of the received signal, we set $s_{A-M\lambda_1}(t)$ as a quadrature amplitude modulation - 16 (QAM-16) signal (see, [34], pp. 29 and 102; [32], Eqs. (8) and (9); [35], Eq. (35); [36], Chap. 6). In the ideal scenario without turbulence, the system's BER is mainly affected by the bandwidth and noise of the detector. For high-speed signals, the BER is obtained by thresholding the received signal and accumulating statistics over a long period of time. Therefore, under equivalent SNR, the analysis can be conducted employing equivalent low-speed signals as experimental samples. Considering that the frequency of turbulence disturbances is less than 100 Hz level, the signals generated by the turbulence disturbance model in this paper are continuous sequences in the spatiotemporal domain with millisecond coherence times [37]. They

Optics EXPRESS

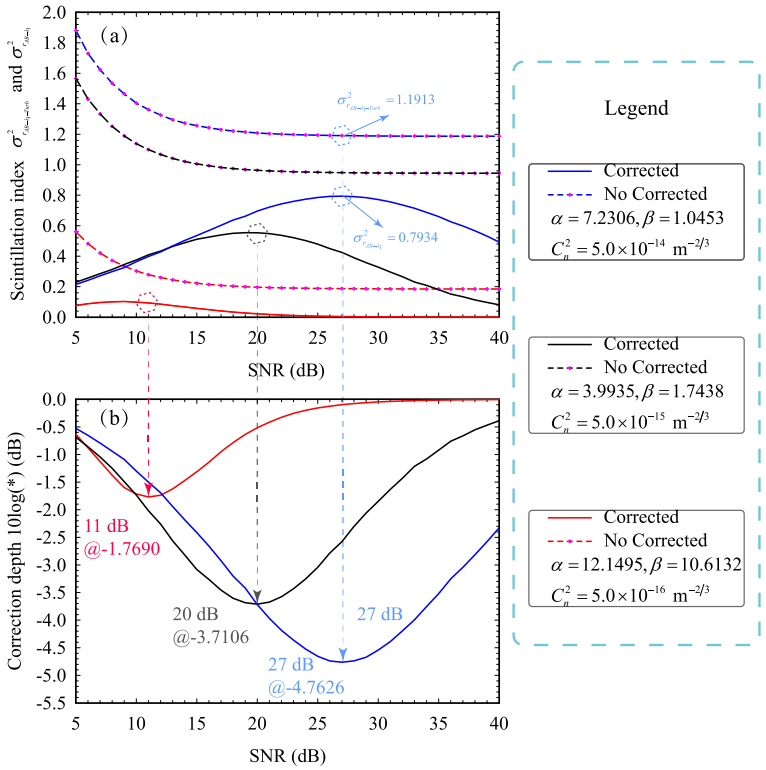

Fig. 6. SI performances of reciprocity optical signal sequences at Alice and Bob after OAPC calibration under different turbulences and SNRs. (a) Correction and non-correction; (b) correction depth χ_{dB}. Blue, black, and red lines denote $C_n^2 = 5 \times 10^{-14}$ m$^{-2/3}$, $\alpha = 7.2306$, $\beta = 1.0453$; $C_n^2 = 5 \times 10^{-15}$ m$^{-2/3}$, $\alpha = 3.9935$, $\beta = 1.7438$; and $C_n^2 = 5 \times 10^{-16}$ m$^{-2/3}$, $\alpha = 12.1495$, $\beta = 10.6132$. The four optical wavelengths are $\lambda_1 = 1555.75$ nm, $\lambda_2 = 1554.13$ nm, $\lambda_3 = 1552.52$ nm, and $\lambda_4 = 1548.51$ nm, respectively. The propagation distance, the transverse wind speed, and sampling delay time represent $L = 5000$ m, $v_\perp = 1$ m/s, and $\tau_d = 0$.

are 6.4 ms, 26.0 ms, and 35.2 ms, respectively, corresponding to the disturbance frequencies of 156.25 Hz. 38.4615 Hz, 28.4091 Hz, as shown in Figs. 2(a)-(c). In order to capture the BER more easily and increase the detection resolution, the BER statistics are calculated for the information transmitted from Allice to Bob in 1 second of the 16-QAM signal, and the number of samples is taken as 1000. The number of symbols in 1 second of the continuous signal $s_{A-M\lambda_1}(t)$ is set to 1.0×10^6 bit, and the up-sampling frequency is set to 4 times the symbol rate, with a raised cosine filter of 0.025 roll-off factor. According to Eqs. (25)–(26), we plot the PDF and constellation diagram distributions of $r_{AB-\lambda_1-Turb}(t)$ and $r_{AB-\lambda_1}(t)$ under different turbulences for $SNR = 25$ dB in Fig. 7. Where the sampling time delay $\tau_d = 0$ ms, and the received optical signal is mean normalized $I/\langle I \rangle$. As the turbulence intensity increases, the peak of the PDF of $r_{AB-\lambda_1-Turb}(t)$ moves closer to the Y-axis. However, the peak value of the PDF of the auto gain corrected signal $r_{AB-\lambda_1}(t)$ tends to be more biased towards "1" as the turbulence level decreases, at weak turbulence, i.e., there is

$$\arg \mathrm{Max} \left\{ PDF \left(r_{AB-\lambda_1}(t) \right) \right\} \to 1. \tag{27}$$

Optics EXPRESS

Equation (27) indicates that the corrected envelope signal $r_{AB-\lambda_1}(t)$ theoretically should be a stable power line without optical intensity scintillation, as the PDFs shown in Figs. 7(a)-(c). The phenomena depicted in Figs. 5 and 6 are also substantiated.

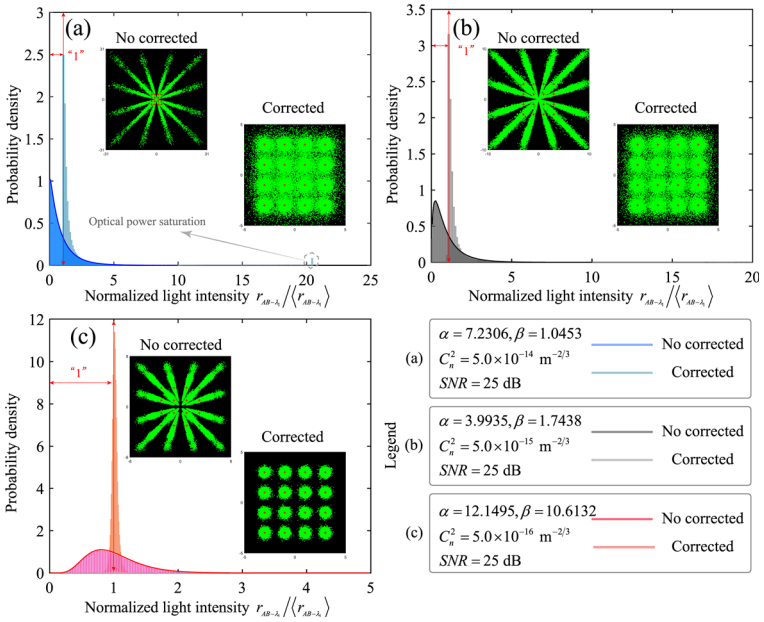

Fig. 7. PDF and constellation performances of reciprocity optical signal sequences at Alice and Bob after OAPC calibration under different turbulences. (a) $C_n^2 = 5\times10^{-14}$ m$^{-2/3}$, $\alpha = 7.2306$, $\beta = 1.0453$; (b) $C_n^2 = 5\times10^{-15}$ m$^{-2/3}$, $\alpha = 3.9935$, $\beta = 1.7438$; and (c) $C_n^2 = 5\times10^{-16}$ m$^{-2/3}$, $\alpha = 12.1495$, $\beta = 10.6132$. The four optical wavelengths are $\lambda_1 = 1555.75$ nm, $\lambda_2 = 1554.13$ nm, $\lambda_3 = 1552.52$ nm, and $\lambda_4 = 1548.51$ nm, respectively. The propagation distance, the transverse wind speed, sampling delay time and system SNR represent $L = 5000$ m, $v_\perp = 1$ m/s, $\tau_d = 0$ and $SNR = 25$ dB, respectively.

It is worth noting that under strong turbulence $C_n^2 = 5\times10^{-14}$ m$^{-2/3}$, there is a protrusion at point $r_{AB-\lambda_1}/\langle r_{AB-\lambda_1}\rangle = 20.3803$, as shown in Fig. 7(a). At this point, the corrected signal $r_{AB-\lambda_1}(t)$ reaches its maximum gain, causing the optical power to reach the saturation state of the detector, thus validating Eqs. (23)–(24). Additionally, by observing the constellation diagram, we know that the communication signals $r_{AB-\lambda_1-Turb}(t)$ after the matched filter and downsampling deviates more and more from the theoretical value as the degree of turbulence increases, leading to an increase in the degree of data point jitter and a deterioration in the BER. The BER deterioration is greatly improved by utilizing $\mu_{A-\lambda_4}(t)$ for OAPC correction. (e.g., strong turbulence $C_n^2 = 5\times10^{-14}$ m$^{-2/3}$, $\log_{10}(\text{BER})$=-0.6842 $\xrightarrow{\downarrow 1.2958}$ $\log_{10}(\text{BER}) = -1.98$; medium turbulence $C_n^2 = 5\times10^{-15}$ m$^{-2/3}$, $\log_{10}(\text{BER})$=-0.8945 $\xrightarrow{\downarrow 1.3755}$ $\log_{10}(\text{BER}) = -2.27$; weak turbulence $C_n^2 = 5\times10^{-16}$ m$^{-2/3}$, $\log_{10}(\text{BER})$=-1.0925 $\xrightarrow{\downarrow 4.507}$ $\log_{10}(\text{BER}) = -5.7$) as shown in the constellation diagrams in Figs. 7(a)-(c). Meanwhile, the BER of the OAPC signal $r_{AB-\lambda_1}(t)$ for different modulation orders M under three turbulence and SNRs are investigated, as depicted in Fig. 8. Where M is set to be $M = 32$ and $M = 16$, the sampling time delay $\tau_d = 0$ ms. The theoretical curves in Fig. 8 are plotted according to Ref. [38] (see, Eqs. (7)–(8), (21)–(22)).

It can be observed that the BER deterioration is greatly moderated by using $\mu_{A-\lambda_4}(t)$ auto gain correction, and the stronger the turbulence, the better the correction effect. For instance, when $M = 16$ and BER reaches forward error correction (FEC) threshold 3.8×10^{-3}, the

Optics EXPRESS

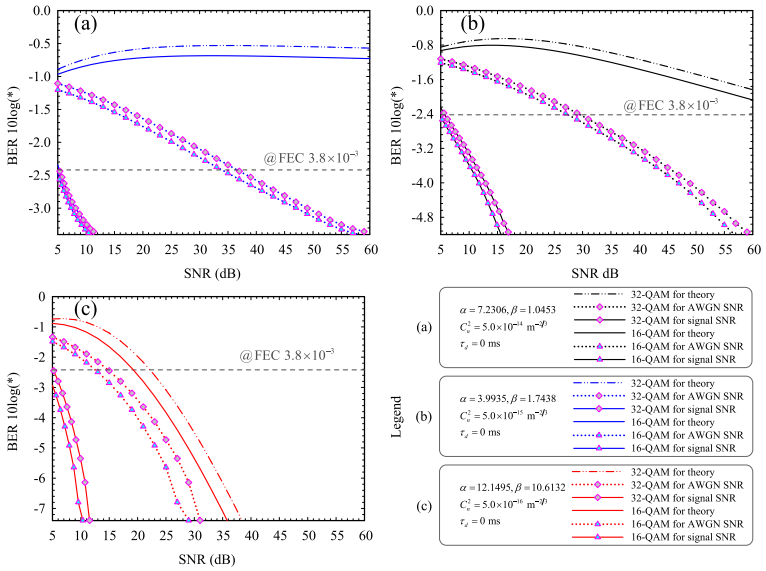

Fig. 8. BER performances of reciprocity optical signal sequences at Alice and Bob after OAPC calibration under different turbulences and SNRs. (a) $C_n^2 = 5 \times 10^{-14}$ m$^{-2/3}$, $\alpha = 7.2306$, $\beta = 1.0453$; (b) $C_n^2 = 5 \times 10^{-15}$ m$^{-2/3}$, $\alpha = 3.9935$, $\beta = 1.7438$; and (c) $C_n^2 = 5 \times 10^{-16}$ m$^{-2/3}$, $\alpha = 12.1495$, $\beta = 10.6132$. The four optical wavelengths are $\lambda_1 = 1555.75$ nm, $\lambda_2 = 1554.13$ nm, $\lambda_3 = 1552.52$ nm, and $\lambda_4 = 1548.51$ nm, respectively. The propagation distance, the transverse wind speed, and sampling delay time represent $L = 5000$ m, $v_\perp = 1$ m/s, and $\tau_d = 0$, respectively.

$\log_{10}$(BER) decreases by 1.72, 1.45, and 1.147 (i.e, BER decreases by 1.72, 1.45, and 1.147 orders of magnitude)under the strong turbulence $C_n^2 = 5 \times 10^{-14}$ m$^{-2/3}$, medium turbulence $C_n^2 = 5 \times 10^{-15}$ m$^{-2/3}$, and weak turbulence $C_n^2 = 5 \times 10^{-16}$ m$^{-2/3}$, respectively. Furthermore, when $M = 32$, all the BER curves shift to the right, indicating that under the same conditions, the BER performance of $M = 16$ is superior to $M = 32$, as shown in Figs. 8(a)-(c). It should be noted here that we define two types of SNR here, one is QAM for AWGN and the other is obtained by performing complex calculations on the received signal and the source signal, as shown in Eq. (28)

$$SNR_{\mathrm{Sig}} = \frac{\left|r_{AB-\lambda_1}(t)\right|^2}{\left|r_{AB-\lambda_1}(t) - \left(\rho_A s_{A-M\lambda_1}(t) + n_A(t)\right)\right|^2}. \tag{28}$$

SNR_{Sig} can truly reflect the state of the signal, the growth trend (slope of the curve) of SNR_{Sig} is relatively fast compared to SNR, but with the increase of turbulence, the growth trend becomes slower and tends to saturation. It can be deduced from the numerical calculations that under the strong turbulence $C_n^2 = 5 \times 10^{-14}$ m$^{-2/3}$, $SNR_{\mathrm{Sig}} \to 34.8971$ dB; the medium turbulence $C_n^2 = 5 \times 10^{-15}$ m$^{-2/3}$, $SNR_{\mathrm{Sig}} \to 322.2233$ dB; the weak turbulence $C_n^2 = 5 \times 10^{-16}$ m$^{-2/3}$, $SNR_{\mathrm{Sig}} \to 322.2735$ dB. It can be observed that the OAPC method based on reciprocity employed in this paper has significantly improved the signal SNR. However, the OAPC correction capability is limited under strong turbulence conditions and an extreme scenario exists, which is due to the saturation limit of the SI and further validates the situation illustrated in Fig. 6.

When the experimental system is running in real-time, it is difficult to guarantee absolute synchronization between Alice and Bob. Based on Eq. (15) and Fig. 5, The BER performances of reciprocity optical signal sequences at Alice and Bob after OAPC calibration are investigated under different turbulences and sampling delays where $SNR = 50$ dB, as shown in Fig. 9.

Optics EXPRESS

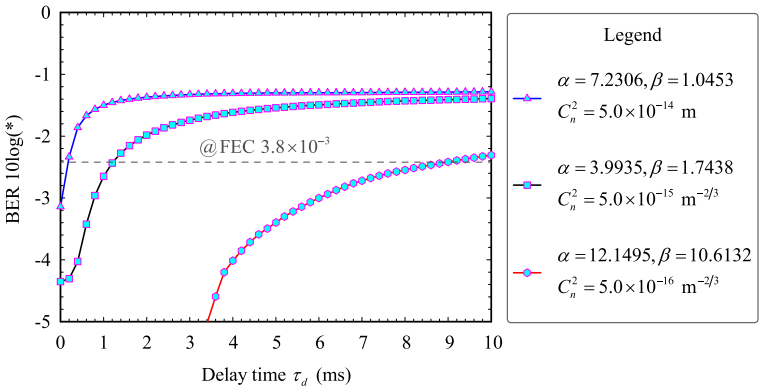

Fig. 9. BER performances of reciprocity optical signal sequences at Alice and Bob after OAPC calibration under different turbulences and sampling delays. (a) $C_n^2 = 5\times10^{-14}$ $m^{-2/3}$, $\alpha = 7.2306$, $\beta = 1.0453$; (b) $C_n^2 = 5\times10^{-15}$ $m^{-2/3}$, $\alpha = 3.9935$, $\beta = 1.7438$; and (c) $C_n^2 = 5\times10^{-16}$ $m^{-2/3}$, $\alpha = 12.1495$, $\beta = 10.6132$. The four optical wavelengths are $\lambda_1 = 1555.75$ nm, $\lambda_2 = 1554.13$ nm, $\lambda_3 = 1552.52$ nm, and $\lambda_4 = 1548.51$ nm, respectively. The propagation distance, the transverse wind speed, and system SNR represent $L = 5000$ m, $v_\perp = 1$ m/s, and $SNR = 50$ dB, respectively.

When the system BER is lower than FEC 3.8×10^{-3}, it is required to have $\tau_d \le 0.186$ ms under strong turbulence $C_n^2 = 5\times10^{-14}$ $m^{-2/3}$, $\tau_d \le 1.129$ ms under medium turbulence $C_n^2 = 5\times10^{-15}$ $m^{-2/3}$ and $\tau_d \le 9.028$ ms under weak turbulence $C_n^2 = 5\times10^{-16}$ $m^{-2/3}$. It illustrates that the BER performance of the OAPC correction system is less tolerant to the sampling desynchronization time as the degree of turbulence increases. As the reciprocity decrease, the corrected scintillation factor and BER deteriorate, which provides another perspective to verify Fig. 5. From the trend of the BER curve shown in Fig. 9, the current 5G and 6G system requirement for keeping the system time delay under the millisecond level is also precisely fulfilled [33].

4. Experimental demonstration and analysis

To further verify the correctness of the previously proposed model, an OAPC experiment system is conducted according to Fig. 1, where the key components in the experiment are shown in Fig. 10. The optical antenna and 3D turntable are used as the transmitting system (see, Fig. 10(a)), and our self-developed turbulence simulator is used to generate turbulence (see, Fig. 10(b)) [39], a high-speed EVOA from Agiltron is used as an adaptive power regulation device with a response rate DC-100 kHz ((see, Fig. 10(c))). Moreover, the FPGA is a Xilinx Spartan-6 XC6SLX9 chip, when performing internal DA and OAPC algorithm, the delay unit is <0.01 ms after the optimization procedure, which can be considered $\tau_d = 0$. The wavelengths $\lambda_1 = 1555.75$ nm, $\lambda_2 = 1554.13$ nm, $\lambda_3 = 1552.52$ nm, and $\lambda_4 = 1548.51$ nm at Alice ends are generated by tunable fiber lasers, corresponding to ports C27, C29, C31, and C36 of DWDM, respectively. Since the structures of Alice and Bob's ends have symmetry, this experiment mainly verifies the OAPC performance of Alice → Bob. Where λ_1 is employed as the carrier of the QAM signal, which generates two RF signals of pseudo random binary sequence (PRBS-15) with 16Gbps through AWG (Keysight M8195A) and drives IQ modulator to generate 64Gbps QAM-16 modulated signal, which is amplified through EDFA (CEFA-C-BO-HP-PM-37-NL1-OM1-M403-FA-FA) and emitted as spatial light through the optical antenna. At Bob, the QAM optical signal passing through the turbulence simulator is received using a DWDM C27 optical antenna, and analyzed using an optical modulation analyzer (Tektronix OM4006D) for mixing, and the signal is

Optics EXPRESS

acquired employing a DSO and analyzed offline. First, we use a low-speed detector (bandwidth DC-200 kHz, minimum detection power −33 dBm, saturation power −8 dBm) at both Alice and Bob to detect the turbulent disturbance signals. The signals from Alice's C36 port λ_4 and Bob's C31 port λ_3 are simultaneously acquired and stored for analysis using an acquisition card with a sampling interval of 1 ms. We compute the real experimental under reciprocity signals with different scintillation indexes offline according to Eq. (20).

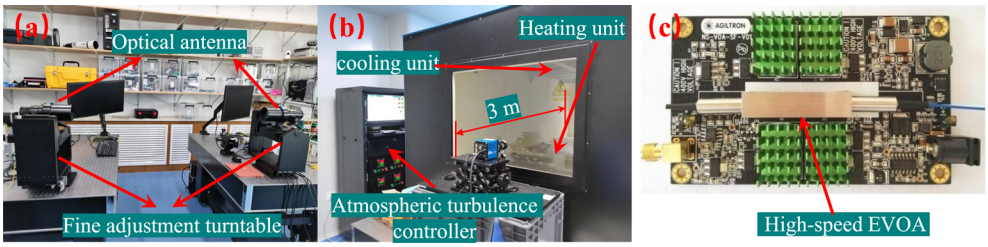

Fig. 10. Experimental main component and hot air convection turbulence simulator. (a) an optical antenna and a 3D turntable; (b) a turbulence simulator with a physical length of 3 m and an equivalent length of 3000 m, which consists of a heating, cooling, and control unit and can simulate an atmospheric coherence length of 0.65 cm- 48 cm; (c) Agiletron's high-speed EVOA with a response rate of DC-100 kHz.

As can be seen from Fig. 11, the mean value of the reciprocity of the experimental system we built keeps above 0.99, which supports the correctness of Eqs. (15) and (16). Furthermore, the QAM-16 communication transmission experiments are performed for verifying the performance of OAPC, as plotted in Fig. 12. The temperature differences of the atmospheric turbulence simulator are set to 20 $^{\circ}C$, 80 $^{\circ}C$, and 150 $^{\circ}C$, corresponding to the atmospheric coherence lengths r_0 of 0.8291 cm, 1.3796 cm, and 4.2404 cm, respectively. The physical path of the atmospheric simulator we developed is 3 m. According to the Ref. [39], the equivalent path we calibrated is 3000 m, and we can equivalently calculate C_n^2 as 1.412×10^{-13} $m^{-2/3}$, 6.0430×10^{-14} $m^{-2/3}$ and 9.4342×10^{-15} $m^{-2/3}$, respectively. When the turbulence intensity is 9.4342×10^{-15} $m^{-2/3}$ and the received power is −32.458 dBm, the BER decreases by an order of 2.8 with OPAC. Under 6.0430×10^{-14} $m^{-2/3}$, 1.412×10^{-13} $m^{-2/3}$ and the received power is −29.971 dBm, −25.163 dBm, the BER decreases by 3.0 and 3.2 orders of magnitude, respectively. As the received power increases, the BER is improved to a greater extent, e.g., when 6.0430×10^{-14} $m^{-2/3}$ and the received power is −21.66 dBm, the BER decreases by 6 orders of magnitude, which are depicted by the green markers in Fig. 12. It can be seen that the overall BER reduction is greater than 2.8 orders of magnitude with the OAPC system, and this trend becomes more pronounced as the received power increases, which also verifies exactly what is shown in Fig. 8. Thus, reciprocity is utilized in this work for transmitter OAPC. There could have important theoretical model parameter reference significance for adaptive optics, adaptive coding, probabilistic shaping, and other advanced coding research using reciprocal systems, as well as adaptive regulation of the intrinsic parameters of communication light beams (such as beam dispersion angle, orbital angular momentum (OAM), etc.) In particular, the components required for the OAPC technique in this paper are all commercially available and standard devices, and the system structure is simple. This could further promote the industrialization and practical application of this technology, and provide new compensation methods for the FSOC BER degradation caused by atmospheric turbulence.

Optics EXPRESS

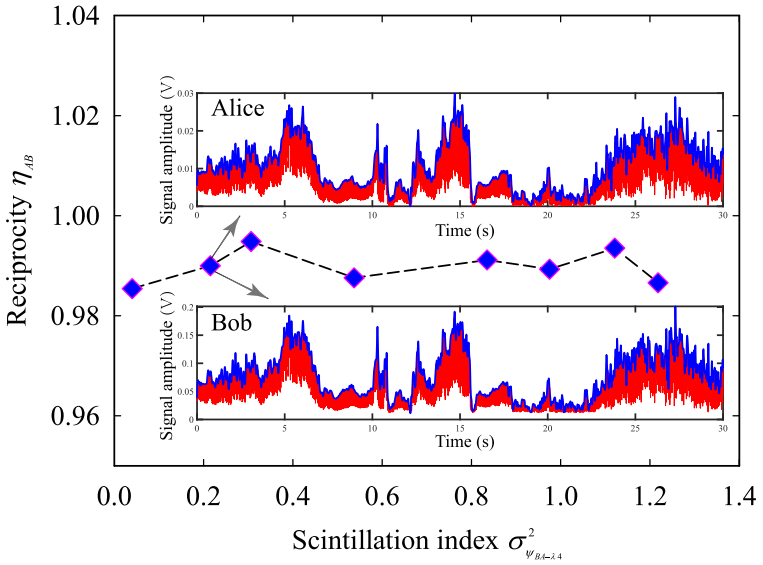

Fig. 11. Reciprocity at different scintillation indexes $\sigma^2_{\psi_{BA-\lambda 4}}$, the average received power of the signal fiber output at Alice and Bod's end for −22 dBm@$\psi_{BA-\lambda_4}$ and −16 dBm@$\psi_{AB-\lambda_3}$, respectively. At $\sigma^2_{\psi_{BA-\lambda 4}}$ = 0.3063, the red and blue lines indicate the acquired signal and signal envelope, respectively. The four optical wavelengths are λ_1 = 1555.75 nm, λ_2 = 1554.13 nm, λ_3 = 1552.52 nm, and λ_4 = 1548.51 nm, respectively.

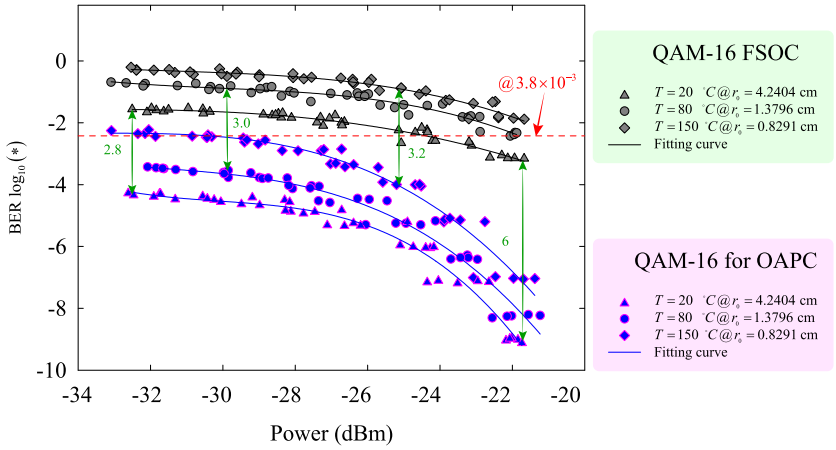

Fig. 12. Experimental statistics for QAM-16 BER performance with and without OAPC under three atmospheric turbulence states, where the three turbulence states are T = 150 °C @ r_0 = 0.8291 cm, T = 80 °C @ r_0 = 1.3796 cm, and T = 20 °C @ r_0 = 4.2404 cm. The four optical wavelengths are λ_1 = 1555.75 nm, λ_2 = 1554.13 nm, λ_3 = 1552.52 nm, and λ_4 = 1548.51 nm, respectively.

5. Conclusion

In this paper, the continuous time-domain OAPC model and control algorithm of FSOC based on atmospheric turbulence channel reciprocity are proposed for mitigating the optical intensity scintillation and communication BER deterioration at the receiver. First, a transmitter OAPC system for atmospheric channel reciprocity is proposed using four adjacent wavelengths in

Optics EXPRESS

the C-band. EVOA and EDFA are employed as the main OAPC units for power adaptation, where DWDM is utilized to distinguish between beacon light for reciprocity monitoring and communication light for transmitting information. Taking into account the delay time and system noise, a reciprocity performance evaluation model for G-G continuous-time signals is derived using the Yule-Worker equation in the ARMA stochastic process, and a reciprocity-based power adaptive control algorithm is proposed. The effects of system noise and sampling asynchrony on the signal reciprocity and the SI performances under OAPC calibration are numerically simulated for strong $C_n^2 = 5\times10^{-14}$ m$^{-2/3}$, medium $C_n^2 = 5\times10^{-15}$ m$^{-2/3}$, and weak $C_n^2 = 5\times10^{-16}$ m$^{-2/3}$ three turbulence intensities. Moreover, the QAM-16 and QAM-32 real-state continuous time-domain signals are fused with the G-G reciprocal turbulent continuous signal model, and the PDF and communication constellation diagram performances after APC correction are analyzed under different turbulence. The BER performances are also discussed at different SNRs and sampling time delays. The numerical simulation results show that G-G reciprocity is maintained at millisecond sampling delay, and the signals are absolutely reciprocal at both receiving ends in hardware configuration and sampling simultaneously. By using reciprocity for OAPC correction, the light intensity scintillation of the communication signal can be well suppressed, and the SNR is substantially improved, and the suppression effect is better under strong turbulence. Considering the actual system operation state, the signal SI suppression degree is 3.5 dB under strong turbulence $C_n^2 = 5\times10^{-14}$ m$^{-2/3}$ when the system noise is in good working performance and sampling delay time $\tau_d = 1$ ms. The QAM-16's BER is reduced by 1.72 orders of magnitude when the BER reaches FEC limit compared with no correction. Finally, a 64 Gpbs QAM-16 OPAC communication experiment was successfully executed by using an atmospheric turbulence simulator and high-speed EVOA (DC-200 kHz). The experimental results show that the overall BER reduction is greater than 2.8 orders of magnitude with the OAPC system, and this trend becomes more pronounced as the received power increases, even reach 6 orders of magnitude in some places.

Funding. National Natural Science Foundation of China (61775022, 62105029, 62105029, 61775022, U2141231, 62275033, U2141231); China Postdoctoral Science Foundation (2021TQ0035, 2021M700415); State Key Laboratory Foundation of Applied Optics (SKLA02022001A11).

Disclosures. The authors declare no conflicts of interest.

Data availability. Data underlying the results presented in this paper are not publicly available at this time but may be obtained from the authors upon reasonable request.

References

1. Y. Zhou, Z. Gu, and J. Zhang, *et al.*, "Efficient deployment of aerial relays in FSO-based backhaul networks," J. Opt. Commun. Netw. **15**(1), 29–42 (2023).
2. A. Misra, C. Kress, and K. Singh, *et al.*, "Reconfigurable and real-time high-bandwidth nyquist signal detection with low-bandwidth in silicon photonics," Opt. Express **30**(8), 13776–13789 (2022).
3. O. Spitz, A. Herdt, and J. Wu, *et al.*, "Private communication with quantum cascade laser photonic chaos," Nat. Commun. **12**(1), 3327 (2021).
4. H. Hemmati, ed., *Near-Earth Laser Communications* (CRC, 2021).
5. S. A. Al-Gailani, M. F. Mohd Salleh, and A. A. Salem, *et al.*, "A survey of free space optics (FSO) communication systems, links, and networks," IEEE Access **9**, 7353–7373 (2021).
6. A. Carrasco-Casado and R. Mata-Calvo, *Space Optical Links for Communication Networks* (Springer International Publishing, Cham, 2020), pp. 1057–1103.
7. M. Toyoshima, "Recent trends in space laser communications for small satellites and constellations," J. Lightwave Technol. **39**(3), 693–699 (2021).
8. A. V. Kudryashov, A. L. Rukosuev, and A. N. Nikitin, *et al.*, "Real-time 1.5 kHz adaptive optical system to correct for atmospheric turbulence," Opt. Express **28**(25), 37546–37552 (2020).
9. J. A. Louthain and J. D. Schmidt, "Synergy of adaptive thresholds and multiple transmitters in free-space optical communication," Opt. Express **18**(9), 8948–8962 (2010).
10. H. Burris, A. Reed, and N. Namazi, *et al.*, "Adaptive thresholding for free-space optical communication receivers with multiplicative noise," in *Proceedings, IEEE Aerospace Conference*, vol. 3 (2002), p. 3.
11. X. Yu, L. Zhang, and Y. Zhang, *et al.*, "2.5 Gbps free-space optical transmission between two 5G airship floating base stations at a distance of 12 km," Opt. Lett. **46**(9), 2156–2159 (2021).

Optics EXPRESS

12. H. Safi, A. A. Sharifi, and M. T. Dabiri, *et al.*, "Adaptive channel coding and power control for practical FSO communication systems under channel estimation error," IEEE Trans. Veh. Technol. **68**(8), 7566–7577 (2019).
13. X. Li, Y. Li, and S. Zhao, *et al.*, "Performance analysis of weather-dependent satellite-terrestrial network with rate adaptation hybrid free-space optical and radio frequency link," Satell. Commun. Network **41**(4), 357–373 (2023).
14. T. Rakia, H. Yang, and F. Gebali, *et al.*, "Power adaptation based on truncated channel inversion for hybrid FSO/RF transmission with adaptive combining," IEEE Photonics J. **7**(4), 1–12 (2015).
15. S. Song, Y. Liu, and T. Xu, *et al.*, "Hybrid FSO/RF system using intelligent power control and link switching," IEEE Photonics Technol. Lett. **33**(18), 1018–1021 (2021).
16. R. Chopra, C. R. Murthy, and H. A. Suraweera, *et al.*, "Blind channel estimation for downlink massive MIMO systems with imperfect channel reciprocity," IEEE Trans. Signal Process. **68**, 3132–3145 (2020).
17. J. Morte Palacios, O. Raeesi, and A. Gokceoglu, *et al.*, "Impact of channel non-reciprocity in cell-free massive MIMO," IEEE Wireless Commun. Lett. **9**(3), 344–348 (2020).
18. J. H. Shapiro and A. L. Puryear, "Reciprocity-enhanced optical communication through atmospheric turbulence - part I: Reciprocity proofs and far-field power transfer optimization," J. Opt. Commun. Netw. **4**(12), 947–954 (2012).
19. A. L. Puryear, J. H. Shapiro, and R. R. Parenti, "Reciprocity-enhanced optical communication through atmospheric turbulence- part II: Communication architectures and performance," J. Opt. Commun. Netw. **5**(8), 888–900 (2013).
20. J. H. Shapiro, "Reciprocity of the turbulent atmosphere*," J. Opt. Soc. Am. **61**(4), 492–495 (1971).
21. Y. Hong, G. Li, and Z. Liu, "Optical adaptive power transmission using APC-EDFA for turbulence-tolerant FSO communications," Opt. Express **29**(15), 23777–23785 (2021).
22. Y. Hong, W. Shin, and S. Han, "APC-EDFA-based scintillation-suppressed photodetection in satellite optical communication," Microw. Opt. Technol. Lett. **61**(10), 2427–2433 (2019).
23. R. R. Parenti, J. M. Roth, and J. H. Shapiro, *et al.*, "Experimental observations of channel reciprocity in single-mode free-space optical links," Opt. Express **20**(19), 21635–21644 (2012).
24. J. Minet, M. A. Vorontsov, and E. Polnau, *et al.*, "Enhanced correlation of received power-signal fluctuations in bidirectional optical links," J. Opt. **15**(2), 022401 (2013).
25. D. Giggenbach, W. Cowley, and K. Grant, *et al.*, "Experimental verification of the limits of optical channel intensity reciprocity," Appl. Opt. **51**(16), 3145–3152 (2012).
26. H. Yao, C. Chen, and X. Ni, *et al.*, "Analysis and evaluation of the performance between reciprocity and time delay in the atmospheric turbulence channel," Opt. Express **27**(18), 25000–25011 (2019).
27. H. Yao, M. Cong, and Z. Liu, *et al.*, "Experimental demonstration of atmospheric channel reciprocity in fiber receiving systems," in *2019 18th International Conference on Optical Communications and Networks (ICOCN)*, (2019), pp. 1–3.
28. C. Chen, H. Yang, and S. Tong, *et al.*, "Mean-square angle-of-arrival difference between two counter-propagating spherical waves in the presence of atmospheric turbulence," Opt. Express **23**(19), 24657–24668 (2015).
29. C. Chen and H. Yang, "Correlation between light-flux fluctuations of two counter-propagating waves in weak atmospheric turbulence," Opt. Express **25**(11), 12779–12795 (2017).
30. L. Binh, *Optical Fiber Communication Systems with MATLAB® and Simulink® Models, Second Edition*, Optics and Photonics (Taylor & Francis, 2014).
31. H. Yao, Q. Hao, and C. Chen, *et al.*, "Generation of temporal fading envelope sequences for the FSOC channel based on atmospheric turbulence optical parameters," Opt. Express **30**(19), 34519–34532 (2022).
32. H. Yao, X. Ni, and C. Chen, *et al.*, "Performance of M-PAM FSO communication systems in atmospheric turbulence based on APD detector," Opt. Express **26**(18), 23819–23830 (2018).
33. P. Torres-Ferrera, F. Effenberger, and M. S. Faruk, *et al.*, "Overview of high-speed TDM-PON beyond 50 Gbps per wavelength using digital signal processing [invited tutorial]," J. Opt. Commun. Netw. **14**(12), 982–996 (2022).
34. H. Kaushal, V. Jain, and S. Kar, *Free space optical communication* (Springer, 2017).
35. H. Yao, X. Ni, and C. Chen, *et al.*, "Performance analysis of MPSK FSO communication based on the balanced detector in a fiber-coupling system," IEEE Access **7**, 84197–84208 (2019).
36. Z. Ghassemlooy, W. Popoola, and S. Rajbhandari, *Optical wireless communications: system and channel modelling with Matlab®* (CRC, 2019).
37. F. P. Guiomar, A. Lorences-Riesgo, and D. Ranzal, *et al.*, "Adaptive probabilistic shaped modulation for high-capacity free-space optical links," J. Lightwave Technol. **38**(23), 6529–6541 (2020).
38. K. P. Peppas and C. K. Datsikas, "Average symbol error probability of general-order rectangular quadrature amplitude modulation of optical wireless communication systems over atmospheric turbulence channels," J. Opt. Commun. Netw. **2**(2), 102–110 (2010).
39. B. Li, H. Yao, and L. Zhang, *et al.*, "32 Gbps QPSK optical communication technology based on a new equalizer in atmospheric turbulence," IEEE Access **9**, 130751–130757 (2021).